FORUM GEOGRAFI
ISSN: 0852-0682 | E-ISSN: 2460-3945

Research article

GIS-Based Ecological Vulnerability Assessment in a Mountainous Region: the Charvak Reservoir, Uzbekistan

Khasan Magdiev[1,2], Dilbarkhon Fazilova[1,3*], Mirshodjon Makhmudov[1], Aziz Kazakov[1,3]

[1] Ulugh Beg Astronomical Institute of the Uzbekistan Academy of Sciences, Tashkent, 100052, Republic of Uzbekistan; [2] Ministry of Economy and Finance of the Republic of Uzbekistan, Tashkent, 100017, Republic of Uzbekistan; [3] Tashkent State Technical University named after Islam Karimov, Tashkent, 100095, Republic of Uzbekistan.

*) Correspondence: dil_faz@yahoo.com

Citation:

Magdiev, K., Fazilova, D., Makhmudov, M., & Kazakov, A. (2026). GIS-based Ecological Vulnerability Assessment in a Mountainous Region: the Charvak Reservoir, Uzbekistan. Forum Geografi. 40(1), 57-72.

Article history:
Received: 25 October 2025
Revised: 2 February 2026
Accepted: 23 February 2026
Published: 27 February 2026

Abstract

Mountain reservoirs in steep terrain face geomorphic, hydrological, and development pressures, yet vulnerability maps can be hard to interpret in terms of drivers. An ecological vulnerability index (EVI) is developed for the Charvak Reservoir basin (Uzbekistan) from three subindices: topographic–geological risk index (TGRI; slope, lithological resistance, soil organic carbon, and distance to active faults), hydrological–ecological risk index (HERI; shoreline proximity and normalized difference water index (NDWI) trend risk, excluding the trend term in a nearshore band to reduce shoreline artifacts), and climatic–anthropogenic risk index (CARI; trends in the normalized difference vegetation index [NDVI], normalized difference built-up index [NDBI], and land surface temperature [LST], plus proximity to infrastructure). May–August Landsat Collection 2 composites (2000–2023) yield trends; indicators are scaled to 0–1 and aggregated using analytic hierarchy process (AHP) weights. Hotspots cluster on reservoir-facing slopes and access valleys; the subindices separate topographic controls from shoreline and corridor pressures. Changes in 2018–2023 show limited class transitions, whereas a 2030 scenario (extrapolated NDVI/NDBI plus shoreline and infrastructure stressors) increases high–very high vulnerability by ~39 km^2 (~3.2 percentage points), mainly in shoreline belts and development corridors. The framework supports zoning and planning in reservoir basins.

Keywords: Anthropogenic Disturbance; Shoreline Dynamics; Built-Up Expansion; Landsat Trend Analysis; Multicriteria Decision Analysis.

1. Introduction

Mountain regions are highly sensitive to interacting climatic variability, steep topography, active tectonics, and intensifying land use pressure (Dainese *et al.,* 2024; Yu *et al.,* 2023). In the Intergovernmental Panel on Climate Change framework, vulnerability reflects the interplay of exposure, sensitivity, and adaptive capacity (Estoque *et al.,* 2023; Hyman *et al.,* 2025). Ecological vulnerability indicates the degree to which ecosystems are exposed and sensitive to external stressors under limited adaptive capacity (Kamran & Yamamoto, 2023). Built-up expansion and transport corridors increasingly coincide with the decrease in vegetation, which highlights that anthropogenic disturbance alongside biophysical constraints must be considered (Chouari, 2024). In Central Asian "water tower" mountains, where seasonal snowmelt governs summer flows, mounting scarcity and interannual variability sharpen management challenges for reservoir basins (Salokhiddinov *et al.,* 2025). Consistently, recent studies document evolving hydrological extremes in mountain reservoirs and glacier cover controls on catchment response in the Tien Shan and High Mountain Asia (Jia *et al.,* 2024; Yun *et al.,* 2025; Zhu *et al.,* 2023).

Reservoir-influenced mountain basins remain underrepresented in ecological vulnerability assessments, despite recurring shoreline fluctuations, steep slope systems, and accelerating land use change (Dainese *et al.,* 2024; Hyman *et al.,* 2025; Liu *et al.,* 2024; Mandal *et al.,* 2023; Rehman *et al.,* 2024). This gap is pertinent for the Charvak Reservoir region in northeastern Uzbekistan, where steep gradients and active faults intersect with seasonal shoreline dynamics (Fazilova *et al.,* 2025; Fazilova *et al.,* 2026). Regional appraisal has documented numerous landslides in the lower Pskem valley and emphasized vulnerability of downstream infrastructure near the reservoir (Juliev *et al.,* 2019; Rosi *et al.,* 2023; Tacconi Stefanelli *et al.,* 2024). In parallel, recreation-driven development has expanded along the shoreline and access routes, and corridor-focused risk mapping identifies transport links to the basin as loss hotspots, underscoring the relevance of infrastructure proximity (Caleca *et al.,* 2024). Scenario-informed planning is therefore increasingly relevant, and land use/land cover forecasting has already been demonstrated in the broader Charvak–Chatkal context (Alikhanov *et al.,* 2024).

Remote sensing and Geographic Information Systems (GIS) provide reproducible indicators—e.g., normalized difference vegetation index (NDVI), normalized difference water index (NDWI), land surface temperature (LST) metrics/trends, terrain derivatives, and soil organic carbon (SOC) layers—enabling basin-scale appraisal in data-limited mountains (Ding & Chen, 2025; Li *et al.,* 2024; Xu *et al.,* 2025; Ye *et al.,* 2022). Recent applications increasingly rely on cloud-based time-series processing and Landsat Collection-2 Level-2 workflows to ensure cross-sensor continuity (Darabi *et al.,* 2025; Kurnianto *et al.,* 2024; Kassahun & Workineh, 2025; Xu *et al.,* 2024). A central methodological issue is how to integrate heterogeneous indicators when validated inventories are scarce. Data-driven models can be powerful but typically require reliable event inventories that are rarely available in remote mountain regions (Chauhan *et al.,* 2025; Khuc *et al.,* 2023). Multicriteria decision analysis (MCDA) approaches—particularly analytic hierarchy process (AHP)—remain attractive for transparent weighting and interpretability within GIS-based composite mapping (Niyogakiza & Liu, 2025; Saha *et al.,* 2022; Wei *et al.,* 2023; Wu *et al.,* 2022), whereas sensitivity to weighting choices is increasingly recognized (Samsuddin *et al.,* 2025). Comparable multifactor schemes have also been applied in mountainous erosion susceptibility mapping with transparent factor selection and validation (Agli *et al.,* 2024), and multidecadal satellite records enable trend-informed indicators relevant for planning (Estacio *et al.,* 2024; Hyman *et al.,* 2025; Luo *et al.,* 2023).

Recent ecological vulnerability assessment studies provide an important benchmark for multifactor mapping and change analysis. AHP-driven conceptual frameworks remain widely used for transparent weighting and index construction (Hu *et al.,* 2021). Remote-sensing vulnerability indices at regional scale highlight the role of land use and infrastructure pressure in shaping vulnerability pattern (Wu *et al.,* 2021). Hybrid modeling strategies further emphasize combining multiple drivers to improve interpretability (Dossou *et al.,* 2021). Spatiotemporal evolution analyses over major plateaus and river basins demonstrate how vulnerability patterns shift through time under coupled environmental and human drivers (Xia *et al.,* 2021; Zhang *et al.,* 2022; Zhang *et al.,* 2025). However, reservoir-affected mountain basins require explicit treatment of shoreline influence and access-corridor pressures and a planning-oriented representation of near-term change. This study addresses that need via a reproducible AHP–GIS workflow that combines multidecadal retrospective appraisal with a baseline-anchored scenario stress test to support basin-scale zoning and management.

Accordingly, a reproducible GIS-based ecological vulnerability model is developed for the Charvak Reservoir basin using AHP weighting and weighted linear aggregation to derive a composite ecological vulnerability index (EVI). Indicators are organized into three domains representing distinct driver groups: topographic–geological predisposition, hydrological–ecological stress, and climatic–anthropogenic pressure, consistent with domain-structured vulnerability applications (Coelho *et al.,* 2024; Terán-Gómez *et al.,* 2025). Alongside the composite EVI, three corresponding domain subindices are reported—topographic–geological risk index (TGRI), hydrological–ecological risk index (HERI), and climatic–anthropogenic risk index (CARI)—computed as weighted sums of the normalized indicators within each domain using AHP-derived local weights (renormalized within-domain).

The framework (i) specifies a three-domain indicator system (TGRI: slope, lithological resistance, fault proximity, SOC; HERI: shoreline proximity and NDWI trend risk; CARI: NDVI, NDBI, and LST trend risks and infrastructure proximity); (ii) applies orientation-consistent normalization to [0,1] and AHP consistency checks; (iii) produces a trend-informed retrospective assessment for 2000–2023 (May–August); and (iv) quantifies observed EVI change for 2018–2023 and a baseline-anchored 2030 scenario, where NDVI and NDBI are extrapolated from 2023 using long-term warm-season trends (2000–2023), whereas hydrological pressure is represented through shoreline proximity and a shoreline-shift stress test. Fixed 2018 quantile thresholds enable class-consistent comparison and transition accounting for observed and scenario periods. Implemented end-to-end in Google Earth Engine, the workflow is reproducible and transferable to other reservoir-affected mountain basins.

2. Methods

2.1. Study Area

The study area is the Charvak Reservoir basin in Tashkent Region, western Tien Shan, northeastern Uzbekistan (41.5–41.9° N, 69.8–70.5° E). The analysis window spans ~1,280 km^2 centered on the reservoir. Relief is rugged, rising from ~650 m at the shoreline to >3,500 m in the Chatkal, Ugam, and Pskem ranges; steep reservoir-facing slopes contribute to high susceptibility to slope instability (Figure 1). The Charvak basin occupies a tectonically active sector of the western Tien Shan where contrasting lithologies and relief combine with steep valley networks. Uplands are predominantly Paleozoic crystalline and sedimentary rocks, whereas foreland and intramontane zones include Neogene–Quaternary successions; extensive loess mantles are common and are known to lose strength upon wetting, contributing to slope instability. Regionally compiled geological mapping and active-fault datasets document major fault systems transecting the area and provide the structural context for elevated seismicity (Rosi *et al*., 2023).

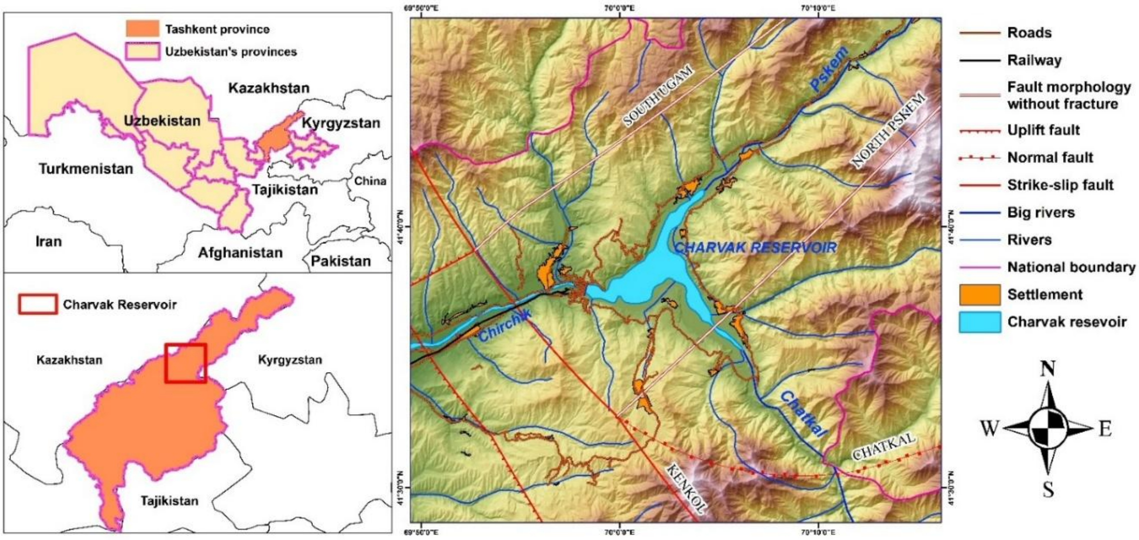

Figure 1. Study Area—Charvak Reservoir Basin (Northeastern Uzbekistan). Hillshade From SRTM (30 m). Faults per Tsay (2019). Roads, Settlements, and Administrative Boundaries From Topographic Maps (1:25,000).

The climate is strongly continental and semiarid; most precipitation falls in November–April, with sharp orographic gradients from the Syr Darya valley (~250–300 mm) to the Pskem valley (~800 mm). Hydrology follows two dominant phases—snow accumulation (October–March) and snowmelt-driven runoff (April–September) (Pachore *et al*., 2024). The Charvak Reservoir is a large multipurpose impoundment that regulates the Chirchik River system; it covers ~40 km^2 with storage on the order of ~2 km^3, and shoreline fluctuations between drawdown and high-water stages locally affect nearshore moisture and bank stability (Juliev *et al*., 2023).

Recent landslide appraisals identified numerous failures in the lower Pskem valley and emphasized the presence of settlements around the artificial lake, underscoring coupled natural and human pressures (Tacconi Stefanelli *et al*., 2024). Downstream of Charvak, the Chirchik–Akhangaran system shows distinct geogenic and anthropogenic solute signatures, reflecting increasing water quality pressure along populated corridors (Fornasaro *et al*., 2024). Recent sediment surveys further indicate potentially toxic elements in recreational riverfront deposits, underscoring exposure risks where tourism intensifies (Fornasaro *et al*., 2025). Regional mapping also identifies the upper Pskem among Central Asian hotspots for landslide-damming susceptibility, relevant for reservoir inlets and valley corridors (Tacconi Stefanelli *et al*., 2024). At regional scale, transport corridors linking the Charvak basin appear as expected-loss hotspots, reinforcing the rationale for including infrastructure proximity in the indicator system (Caleca *et al*., 2024).

Human footprints cluster along reservoir margins and valley floors. In the wider Ugam–Chatkal context adjacent to Charvak, land use/land cover analyses over the last three decades showed measurable built-up expansion and produced scenario-based projections, indicating continued development pressure. Independently, regional risk mapping for Central Asia highlighted road–rail corridors in northeastern Uzbekistan that provide access to the Charvak basin as expected-loss hotspots, reinforcing the need to consider infrastructure proximity in vulnerability appraisals (Alikhanov *et al*., 2024).

2.2. Data Sources and Processing

The workflow produces one composite index (EVI) and three domain-specific subindices (TGRI, HERI, and CARI) corresponding to the topographic–geological, hydrological–ecological, and climatic–anthropogenic domains —computed as AHP-weighted sums of orientation-consistently normalized indicators within each domain to support diagnostic interpretation.

Ten indicators were selected to represent (i) topographic–geological predisposition (slope, lithological resistance, distance to faults, and SOC), (ii) hydrological–ecological stress (shoreline proximity and NDWI trend risk), and (iii) climatic–anthropogenic pressure (NDVI trend risk, NDBI trend risk, distance to infrastructure, and LST trend risk). All datasets were harmonized to Universal Transverse Mercator (UTM) Zone 42N and a 30-m analysis grid; SOC (250 m) was resampled to the common grid. Data sources and processing steps are summarized in Table 1.

Table 1. Indicators Used for Long-Term (2000–2023) EVI Assessment in the Charvak Reservoir Region.

Domain	Indicator	Data source
Topographic–geological	Slope gradient	SRTM DEM (30 m) (NASA SRTM, 2013)
	Lithological resistance	Geological map of Uzbekistan (1:180,000)
	Proximity to faults	Fault database (Tsay, 2019)
	Soil organic carbon (SOC, 0 cm)	OpenLandMap (SOC, USDA-6A1C, v02; 250 m)
Hydrological–ecological	NDWI (trend, 2000–2023)	Landsat 5/7/8/9 (Collection 2, Level-2 SR)
	Distance from reservoir (reference shoreline)	Digitized shoreline from maps (1:25,000)
Climatic–anthropogenic	NDVI (trend, 2000–2023)	Landsat 5/7/8/9 (Collection 2, Level-2 SR)
	NDBI (trend, 2000–2023)	Landsat 5/7/8/9 (Collection 2, Level-2 SR)
	LST (trend, 2000–2023)	Landsat 5/7/8/9 (Collection 2, Level-2 ST)
	Proximity to infrastructure	Digitized roads and tourism facilities from maps (1:25,000)

For the retrospective assessment, warm season (May–August) Landsat Collection 2 Level-2 records (2000–2023) were used to derive trend indicators (NDVI, NDBI, NDWI, and LST), whereas terrain and ancillary layers (slope, lithology, distance to faults, shoreline proximity, and SOC) provided contextual controls. SOC was included as an integrative proxy of soil condition; additional soil properties (e.g., texture or depth) were omitted to limit redundancy with lithology/topography and because harmonized basin-scale layers of comparable reliability are often limited (Salgado *et al.*, 2025). For the near-term component, observed conditions were mapped for 2018 and 2023 using year-specific seasonal composites, and a 2030 scenario was anchored to the 2023 baseline. NDVI and NDBI were extrapolated from 2023 using long-term (2000–2023) warm-season slopes, whereas hydrological pressure was represented by shoreline proximity and a shoreline-shift stress test; the NDWI trend risk layer was retained as a long-term indicator with exclusion of the nearshore band. Following common practice for long time-series analyses, indicators were orientation-normalized so that higher values consistently denote higher vulnerability (Yu *et al.*, 2023).

2.2.1. Topographic–Geological Domain

Slope (°) was derived from the 30 m SRTM DEM (USGS/SRTMGL1_003) and rescaled to [0,1], where steeper slopes correspond to higher ecological vulnerability (Figure 2a; see also Fazilova *et al.*, 2021).

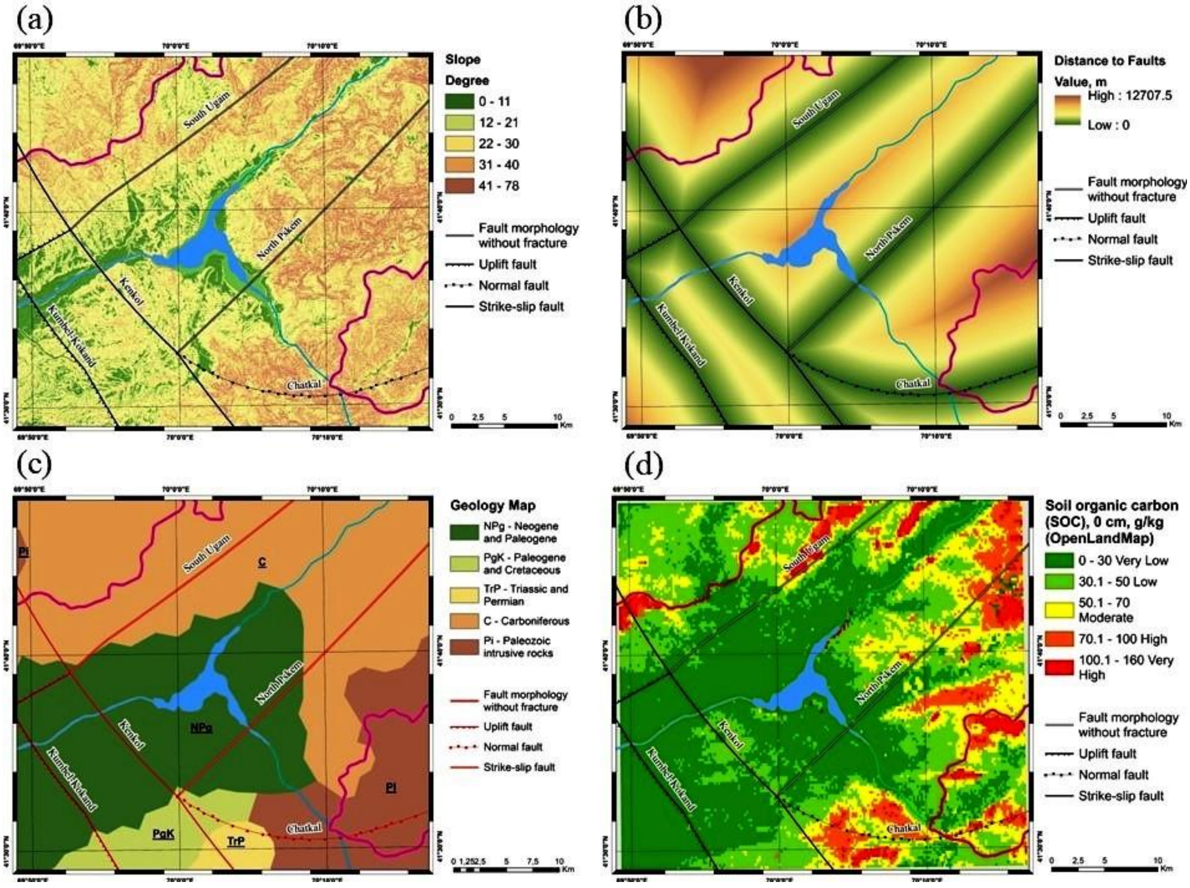

Figure 2. Topographic–Geological Indicators: (a) Slope (°), (b) Distance to Active Faults (m), (c) Lithology, (d) Topsoil Soil Organic Carbon (SOC, g/kg).

Active faults were compiled from regional tectonic maps (Tsay, 2019). A distance-to-fault surface was computed and inverted so that proximity corresponds to higher vulnerability; values were robustly normalized to [0,1] using land-only p2–p98 scaling to reduce outlier influence. Fault proximity was retained as a conditioning factor that can locally weaken rock mass and increase fracture density; however, its contribution was kept moderate (local weight 0.13; global weight 0.052), so that faults act mainly as a spatial modulator rather than a basin-wide dominant driver (Figure 2b).

Lithological units were digitized from regional geological mapping (1:180,000; Drummer, 1998), grouped into resistance classes, and assigned vulnerability scores that were rescaled to [0,1], where lower resistance corresponds to higher vulnerability (Figure 2c).

SOC was obtained from OpenLandMap (250 m) (Hengl & Wheeler, 2018). The surface layer (0 cm reference depth; provided as SOC × 5 g/kg) was converted to g/kg, resampled to the 30 m working grid, and inversely normalized to [0,1] using land-only p2–p98 scaling so that lower SOC corresponds to higher vulnerability (Figure 2d).

2.2.2. Hydrological–Ecological Domain

NDWI was computed from annual warm season (May–August) Landsat Collection 2 Level-2 surface-reflectance composites for 2000–2023 (TM/ETM+/OLI), using QA-based cloud/shadow masking and Collection-2 radiometric scaling prior to index calculation. For each pixel, an ordinary least-squares linear regression was fitted to the annual NDWI series to estimate the 2000–2023 slope. The slope was converted into an NDWI trend risk layer by robust p2–p98 normalization computed on land pixels only and oriented so that persistent drying (more negative NDWI trend) corresponds to higher vulnerability. To suppress mixed land–water artifacts, the NDWI trend risk layer was masked within a nearshore exclusion band (≤150 m) (Zhou *et al.,* 2017) (Figure 3a).

Shoreline proximity was derived from a digitized reservoir polygon. A stable shoreline edge was extracted from the binary water mask using a smoothed morphological gradient (with focal-mode filtering to reduce speckle), and shoreline distance (m) was computed using a fast distance transform. Shoreline proximity was then transformed into a physical “shore-influence” risk layer by linear scaling from 1 at the shoreline to 0 at 1 km (truncated beyond 1 km) (e.g., Ullah *et al.,* 2024) and constrained to [0,1]. This nearshore cap is consistent with the commonly observed short-range dominance of distance-to-water predictors in slope susceptibility, where effects are strongest within the first few hundred meters and typically diminish within a few kilometers (Wang *et al.,* 2024). The HERI combines shoreline proximity and NDWI trend risk with nearshore renormalization: shoreline proximity dominates within the exclusion band, whereas beyond it both components contribute via a weighted combination (Figure 3b).

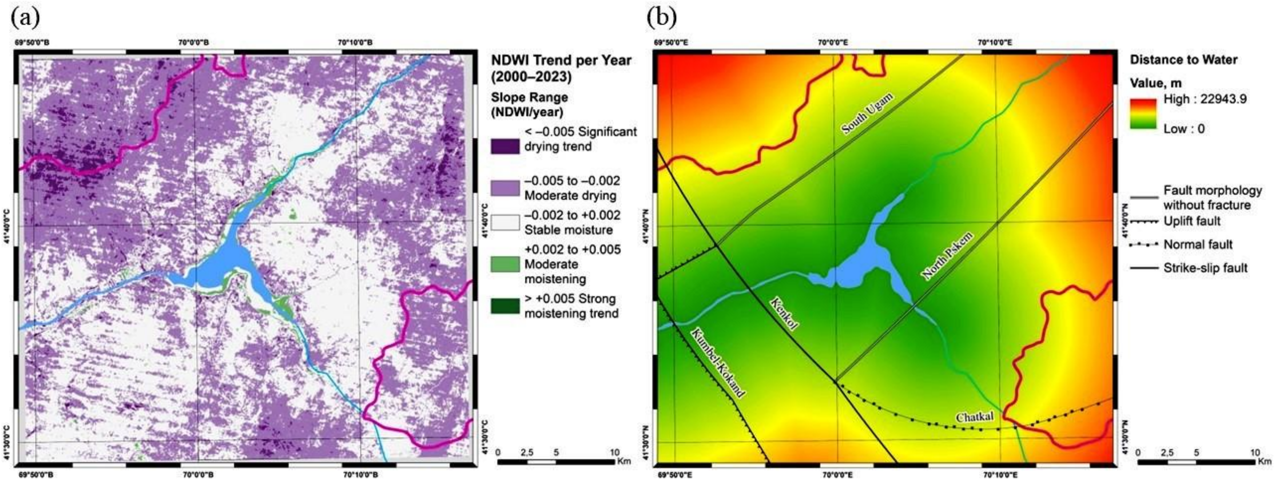

Figure 3. Hydrological–Ecological Indicators: (a) NDWI Trend Slope (2000–2023), (b) Distance to the Reservoir (m).

2.2.3. Climatic–Anthropogenic Domain

This domain operationalizes vegetation trend mapping (NDVI) and built-up expansion (NDBI) alongside proximity to infrastructure and thermal stress expressed by long-term LST trends. Vegetation dynamics were captured by computing NDVI from annual cloud-masked Landsat composites (May–August, Collection 2 Level-2 surface reflectance; TM/ETM+/OLI) NDVI=(NIR-

RED)/(NIR+RED) (Figure 4). Pixel-wise linear trends (2000–2023) were estimated using ordinary least squares and normalized to [0,1] with robust p2–p98 scaling computed on land pixels only, with declining vegetation cover (negative slopes) mapped as higher vulnerability (Figure 4a).

Built-up dynamics were represented using the NDBI, computed as NDBI=(SWIR-NIR)/(SWIR+NIR). Pixel-wise NDBI trends (2000–2023) were derived from annual composites and normalized to [0,1] using land-only p2–p98 scaling, with positive slopes (built-up growth) assigned higher vulnerability to reflect intensifying anthropogenic pressure (Figure 4b).

Proximity to infrastructure was computed as a distance-to-road network surface (m), then inverted and robustly normalized to [0,1] (land-only p2–p98) so that areas closer to infrastructure receive higher vulnerability values (Figure 4c).

LST was derived from Landsat Collection 2 Level-2 surface temperature products for the warm season (May–August) over 2000–2023. QA-masked pixels were composited annually (median), converted to °C using the USGS scaling, and screened using a plausible-temperature filter (−5 to 60 °C). Pixel-wise LST trends were estimated from the annual series using linear regression with a minimum-years criterion (≥12 valid annual observations). Open-water pixels were masked using the reservoir-based land–water mask to avoid mixed land–water thermal responses. The resulting LST trend layer was normalized to [0,1] (land-only p2–p98), with higher warming rates mapped as higher vulnerability (Figure 4d) (Hasan *et al.*, 2025).

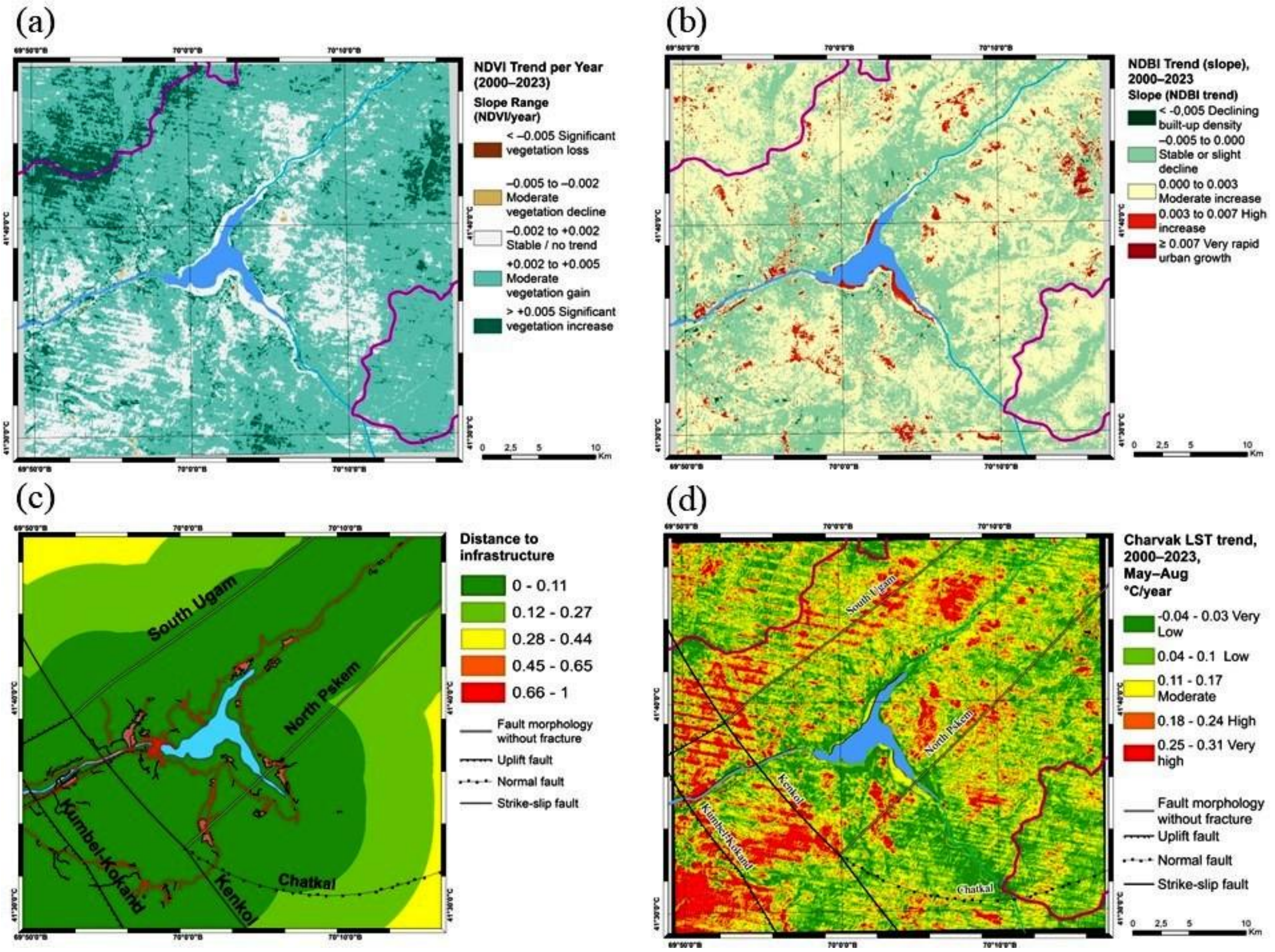

Figure 4. Climatic–Anthropogenic Indicators: (a) NDVI Trend Slope (2000–2023), (b) NDBI Trend Slope (2000–2023), (c) Proximity to Infrastructure (m), and (d) LST Trend Slope (°C/Year; 2000–2023, May–August).

2.3. EVI Construction and Weighting (MCDA–AHP)

An MCDA framework was applied using the AHP to weight indicators within three domains: topographic–geological, hydrological–ecological, and climatic–anthropogenic. The topographic–

geological domain captures terrain and structural predisposition (slope gradient, lithological resistance, proximity to active faults) and soil susceptibility represented by SOC. The hydrological–ecological domain represents reservoir-related stress through shoreline proximity and moisture-change dynamics via NDWI trend. The climatic–anthropogenic domain characterizes vegetation and land use pressure (NDVI and NDBI trends), accessibility/development pressure (proximity to infrastructure), and thermal stress (LST trend).

Indicator weights were derived from expert-based pairwise comparisons using the 1–9 Saaty importance scale. For each domain, a pairwise comparison matrix was constructed and the priority vector (local weights) was computed; consistency was evaluated using the consistency ratio (CR), with CR ≤ 0.10 considered acceptable. Global weights were then obtained as the product of domain (group) weights and local weights and used in the integrated index. The AHP procedure follows the standard formulation and recent AHP–GIS applications in environmental and hazard assessment (Aichi *et al*., 2024; Taoukidou *et al*., 2025). Local (within-domain) and global (Σ = 1.00) weights are reported in Table 2.

All geoprocessing and map algebra were implemented in Google Earth Engine (GEE). Landsat Collection 2 Level-2 scenes (TM/ETM+/OLI from Landsat 8/9) were scaled to surface reflectance using the USGS-provided factors, masked using QA_PIXEL cloud/shadow-related flags, and aggregated to annual warm season (May–August) median composites (USGS, 2024). All rasters were harmonized to UTM Zone 42N (EPSG:32642) on a 30-m grid and transformed to orientation-consistent vulnerability indicators in the [0,1] range using robust normalization where appropriate (e.g., p2–p98 scaling for trend and distance layers).

Directionality was defined so that higher values consistently indicate higher vulnerability (e.g., lower NDVI and more negative NDWI trends → higher vulnerability; higher NDBI and LST warming trends → higher vulnerability; shorter distances to faults, shoreline, and infrastructure → higher vulnerability via inversion of distance surfaces).

Table 2. AHP-Derived Weights for Ecological Vulnerability Indicators in the Charvak Reservoir Region.

Domain	**Indicator**	**Domain weight**	**Local weight**	**Global weight (Domain × Local)**	**References**
Topographic–geological	Slope gradient (G1)	0.400	0.432	0.173	
	Lithology (G2)		0.238	0.095	Fan *et al*., 2025 Liao *et al*., 2022
	Proximity to active faults (distance, G3)		0.130	0.052	
	Soil organic carbon (SOC, G4)		0.200	0.080	El Beyrouthy *et al*., 2025
Hydrological–ecological	NDWI trend (drying trend, H1)	0.200	0.335	0.067	Tesfaye *et al*., 2024
	Proximity to reservoir shoreline (distance, H2)		0.665	0.133	Miura *et al*., 2025
Climatic–anthropogenic	NDVI-based vegetation stress (C1)	0.400	0.156	0.062	Guo *et al*., 2024
	NDBI-based built-up pressure (C2)		0.395	0.158	Arif & Toersilowati, 2024
	Proximity to infrastructure (distance, C3)		0.249	0.100	Fan *et al*., 2025; Liao *et al*., 2022
	LST trend risk (warming trend, C4)		0.200	0.080	Guo *et al*., 2024; Arif & Toersilowati, 2024

Note: References in Table 2 support the selection/relevance and data sources of the indicators; weight values are AHP outputs from expert pairwise comparisons.

The composite EVI was computed as a weighted linear combination, as shown in Equation 1:

$$EVI = \sum_{I=1}^{10} \omega_i I_i \, , \; \sum_{I=1}^{10} \omega_i = 1 \; _{(1)} \qquad (1)$$

where Ii are the normalized indicators and wi are the AHP weights.

For the 2000–2023 retrospective appraisal, EVI and thematic indices (TGRI, HERI, and CARI) are presented as continuous 0–1 rasters; where classed maps are shown, quantile-based breaks (q20, q40, q60, and q80) computed from the land-only distribution of the ranked surface are used to form five classes (1–5).

2.4. Scenario-Based EVI Projection to 2030

A near-term EVI projection to 2030 was generated using a baseline-anchored scenario design. The method combines an observed change component (2018–2023) with a forward scenario component (2023–2030) to produce consistent maps of recent dynamics and potential near-term shifts in geoecological vulnerability. Annual growing-season (May–August) Landsat composites were produced for each year using Collection 2 Level-2 surface reflectance with QA-based cloud/shadow masking and multisensor harmonization (Landsat 5/7/8/9).

For the baseline years (2018 and 2023), NDVI and NDBI were derived from seasonal composites, transformed from the native $-1\ldots1$ domain to 0–1, and oriented to vulnerability (decreasing NDVI and increasing NDBI indicate higher vulnerability). For the 2030 projection, NDVI and NDBI were extrapolated from the 2023 baseline using pixel-wise linear slopes estimated from the long-term record (2000–2023; May–August), computed only where at least 12 valid years are available (Equation 2).

$$X_{2030} = X_{2023} + \beta(2030 - 2023) \tag{2}$$

where X is NDVI or NDBI and β is the annual slope estimated from the long-term growing-season record (2000–2023; May–August) using pixel-wise linear regression, computed only where at least 12 valid years are available. Projected values were clipped to the valid $-1\ldots1$ range and converted to vulnerability-consistent indicators prior to integration with the other layers.

Static and semistatic layers (slope, lithological resistance, distance to active faults, SOC, and baseline shoreline distance), together with long-term NDWI and LST trend layers (2000–2023), retained the same definitions across years unless modified by scenario assumptions. Hydrological–ecological pressure was represented by a renormalized HERI combining shoreline proximity and NDWI trend risk; the NDWI trend component was excluded within a 150 m nearshore band to suppress shoreline-driven artifacts while preserving the physical meaning of shoreline proximity.

A combined-stressor configuration was implemented through three adjustments applied prior to aggregation: (i) infrastructure expansion, represented by buffering roads by 250 m and recomputing proximity-to-infrastructure risk; (ii) high-water shoreline influence, implemented by shifting shoreline distance inward by 100 m before calculating shoreline proximity risk; and (iii) vegetation stress amplification, implemented by multiplying the NDVI-based vulnerability term by 1.2 and constraining it to 0–1.

Percentile-based normalization (p2–p98) for distance and trend layers was computed on land pixels only to prevent water surfaces from biasing scaling ranges. For comparability, domain-rank normalization and five-class thresholds were anchored to the 2018 reference distribution. Five classes were defined by 2018 quantile thresholds (q20, q40, q60, q80) and applied unchanged to 2023 and 2030. Outputs include ranked EVI maps for 2018 and 2023, the scenario-based EVI map for 2030, change maps for 2018–2023 and 2023–2030, class-area summaries, and class-to-class transition matrixes.

3. Results

3.1. Thematic Vulnerability Indices (2000–2023)

The three thematic indices highlight complementary drivers of ecological vulnerability in the Charvak Reservoir basin (Figure 5). The TGRI integrates slope, proximity to active faults, lithology, and soil susceptibility expressed by SOC. The spatial pattern (Figure 5a) shows high–very high values along the reservoir-facing escarpments of North Pskem and across the Kumbel–Kokand–Kenkol sector, where steep terrain coincides with weaker lithological units and lower SOC. Low TGRI dominates comparatively stable upland blocks and sectors under more resistant bedrock. Fault proximity contributes secondary, locally focused amplification of TGRI along mapped structures, consistent with structurally controlled slope weakening and drainage incision.

The HERI combines the NDWI trend risk and shoreline proximity (Figure 5b). High HERI values form a distinct nearshore belt driven primarily by short shoreline distances, whereas the NDWI trend component modulates the interior by elevating areas experiencing persistent drying. As a result, upland sectors away from the shoreline can still map as moderate–high where drying trends are sustained, whereas the immediate reservoir margin remains consistently high due to direct shoreline influence.

The CARI integrates NDVI trend risk, NDBI trend risk, proximity to infrastructure, and LST trend risk (Figure 5c). High CARI patches cluster along development and access corridors and in zones where built-up growth and infrastructure proximity overlap, with additional reinforcement where warming trends are pronounced. In contrast, more remote upland areas tend to remain low where development pressure is limited and vegetation trends are stable.

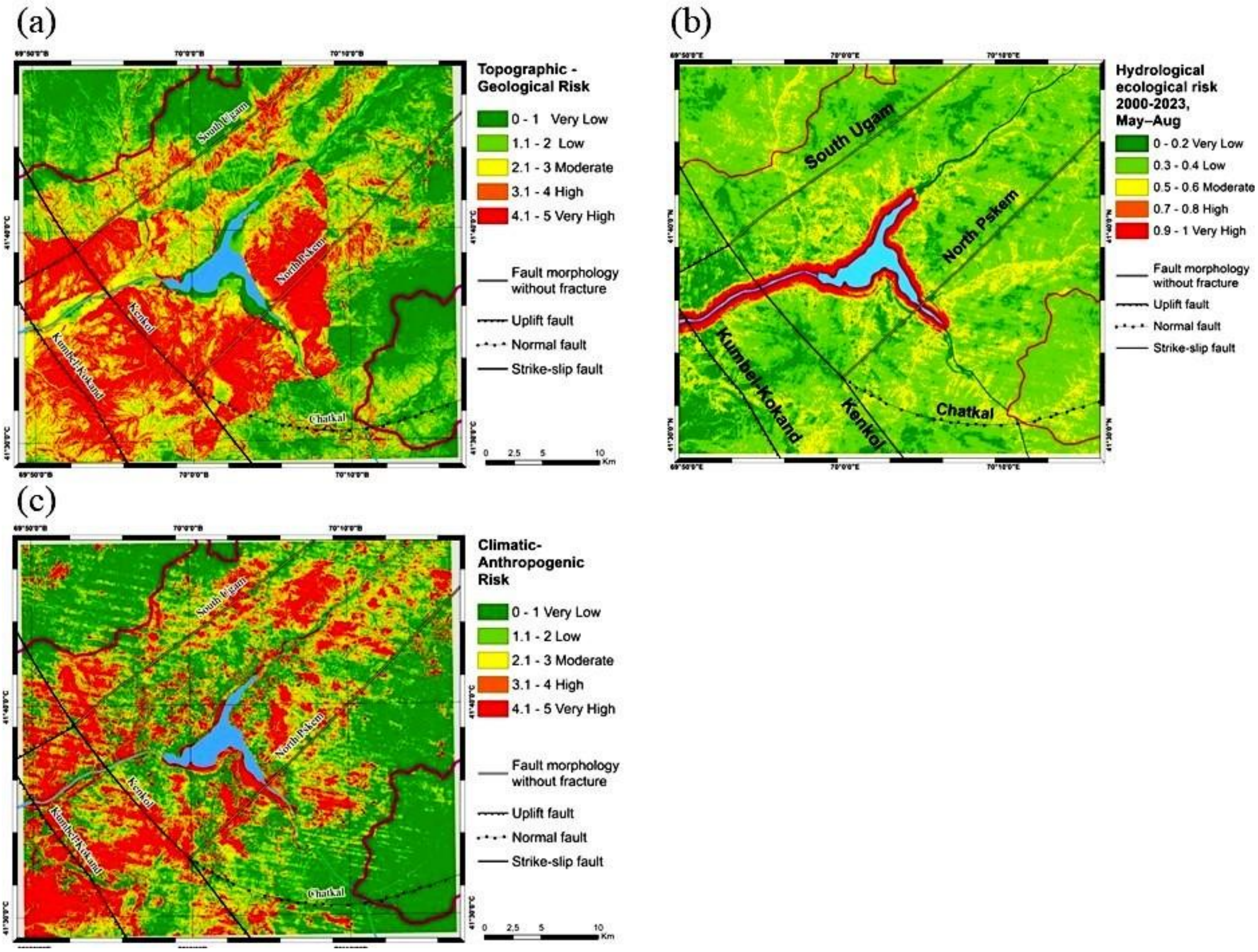

Figure 5. Thematic Ecological Vulnerability Indices for the Charvak Reservoir Region: (a) Topographic–Geological Risk Index (TGRI), (b) Hydrological–Ecological Risk Index (HERI), and (c) Climatic–Anthropogenic Risk Index (CARI).

3.2. Spatial Patterns of EVI (2000–2023)

The five-class EVI map (Very low–Very high) integrates the three thematic domains and reveals coherent spatial structure across the Charvak basin (Figure 6). High–very high vulnerability (classes 4–5) is concentrated in the Kumbel–Kokand–Kenkol sector and along parts of the reservoir-facing North Pskem slopes, forming contiguous hotspots where predisposing conditions and multiple pressures overlap. In contrast, very low–low vulnerability (classes 1–2) is more prevalent across relatively stable uplands and remote interior sectors.

Table 3. Areal Distribution of EVI Classes (2000–2023, May–August).

EVI class	Area (km²)	Share (%)
Very low	269.27	21.01
Low	260.34	20.31
Moderate	243.23	18.98
High	255.90	19.97
Very high	252.86	19.73
Total (land)	1281.60	100.00

Note: Areas Are Reported for Land Pixels Within the Study Area.

The spatial pattern is consistent with the domain indices by design: topographic–geological predisposition (TGRI) dominates where steep slopes and susceptible lithologies occur; HERI is highest in the reservoir-influenced belt and locally in drier interior areas; and CARI increases along accessible development corridors and thermal-stress patches. Global AHP weights indicate that slope and the built-up pressure component are the largest contributors, followed by shoreline proximity and infrastructure proximity, whereas fault proximity has the smallest global weight (Table 2). Class-area proportions for the long-term EVI map are reported in Table 3.

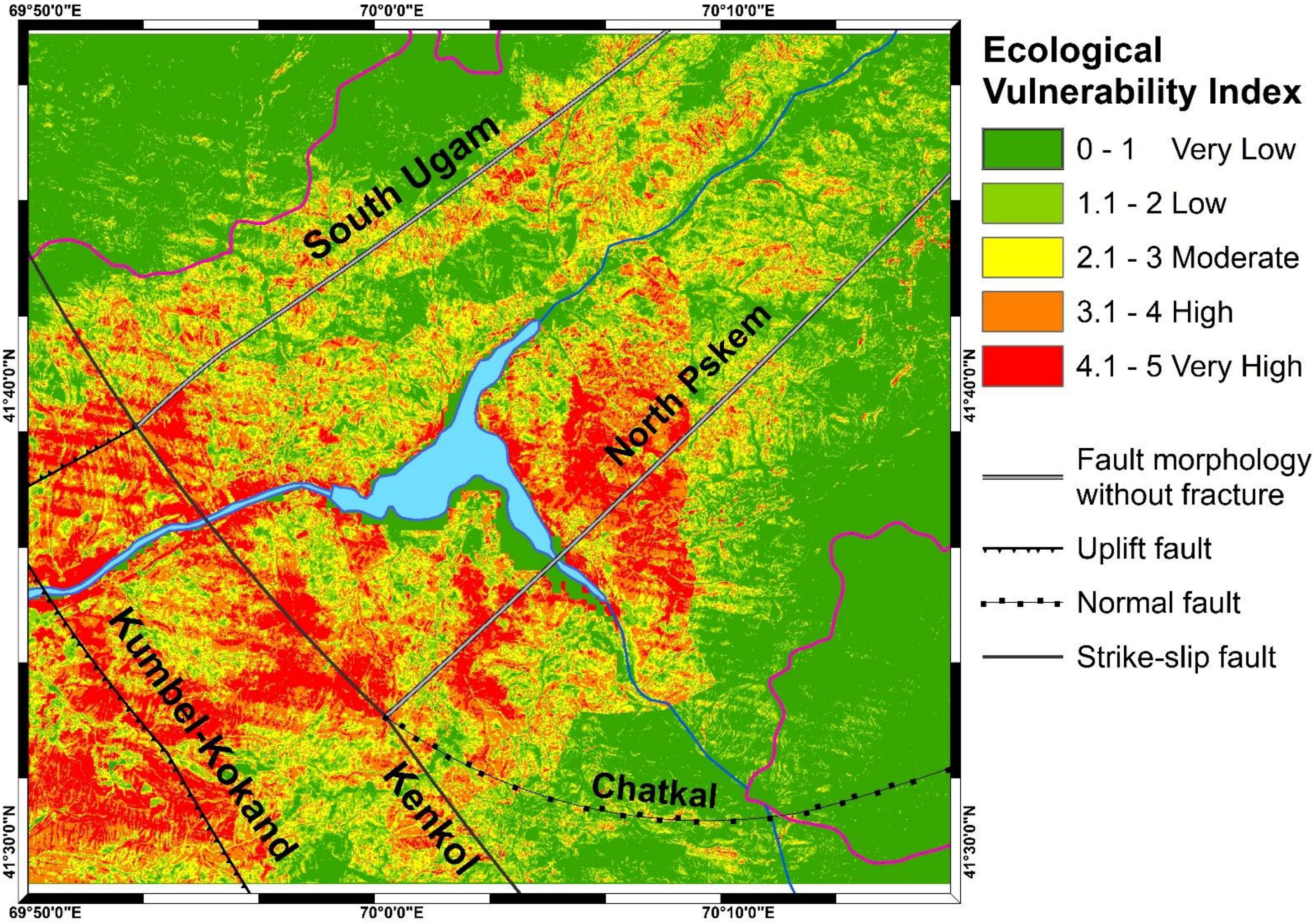

Figure 6. Composite Ecological Vulnerability Index (EVI) for the Charvak Reservoir Basin, 2000–2023 (30 m). Values Are Shown on a 0–1 Scale, Where Higher Values Indicate Higher Vulnerability.

3.3. Observed Change (2018–2023) and 2030 Ccenario Outcomes

Figure 7a shows the 2023 EVI baseline map. For cross-year comparison, EVI was grouped into five classes (Very low to Very high) using fixed class thresholds derived from the 2018 reference distribution. High and very high classes are concentrated along reservoir-facing slopes and major valley corridors, whereas lower classes dominate the interior uplands and upper catchments. Open-water areas are masked. Within the nearshore band (≤150 m), the NDWI trend component is excluded and shoreline proximity governs the hydrological–ecological term, reducing shoreline-related artifacts in the change fields.

Figure 7b shows the observed EVI change between 2018 and 2023. Most of the basin exhibits low-to-moderate change magnitudes, with localized patches of increase and decrease. Class-based transition accounting for this period is summarized in Table 4.

Figure 7c presents the scenario-based EVI change from 2023 to 2030 under the combined-stressor assumptions. The strongest increases are spatially concentrated and follow areas most affected by the imposed shoreline and infrastructure stressors. Scenario transition outcomes are reported in Table 5.

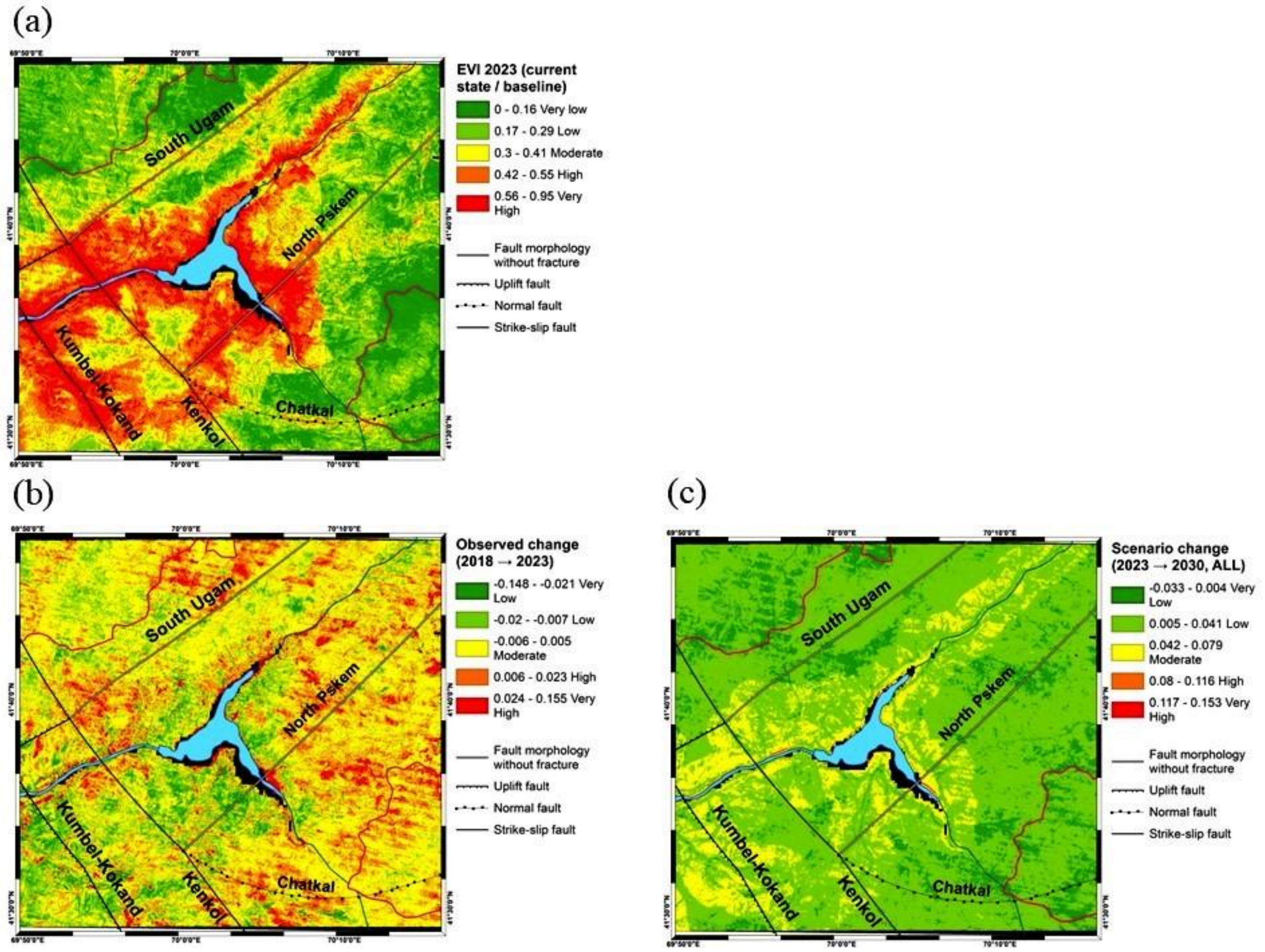

Figure 7. Charvak Basin EVI Maps: (a) EVI 2023 Baseline, (b) Observed Change 2018–2023, (c) Scenario Change 2023–2030 (Combined Stressors).

Table 4. High–Very High (Classes 4–5) Transitions for Observed Change (2018–2023).

Metric	**Area (km²)**	**Share (%)**
Total mapped land area	1247.34	100
High–very high area in 2018 (classes 4–5)	502.55	40.29
High–very high area in 2023 (classes 4–5)	500.43	40.12
Moved to high–very high (1–3 → 4–5)	7.48	0.60
Moved out of high–very high (4–5 → 1–3)	9.60	0.77
Net change in high–very high area from 2018 to 2023 (target − baseline)	-2.11	-0.17

Table 5. High–Very High (Classes 4–5) Transitions Under the 2030 Combined-Stressor Scenario (2023–2030).

Metric	**Area (km²)**	**Share (%)**
Total mapped land area	1247.34	100
High–very high area in 2023 (classes 4–5)	500.43	40.12
High–very high area in 2030 (classes 4–5)	539.83	43.28
Moved to high–very high (1–3 → 4–5)	39.39	3.16
Moved out of high–very high (4–5 → 1–3)	0.00	0.00
Net change in high–very high area from 2023 to 2030 (target − baseline)	+39.39	3.16

Transition statistics were computed on the intersection of valid land pixels for each pair of years; therefore, total mapped land area in Tables 4–5 may differ from the single-date area totals reported in Table 3.

4. Discussion

4.1. Value of Domain Decomposition and Dominant Driver Groups

Domain decomposition improves transparency and interpretability in GIS–MCDA vulnerability mapping. A composite index is useful for zoning, but its compensatory nature can mask why a location attains a high overall score. Reporting the three domain subindices—TGRI, HERI, and CARI—addresses this by separating (i) terrain predisposition, (ii) hydrological–ecological pressure linked to reservoir influence and moisture-related change, and (iii) climatic–anthropogenic pressure associated with vegetation condition, built-up dynamics, accessibility, and thermal stress. This structure supports diagnostic interpretation of hotspots (identifying dominant drivers) and facilitates driver-specific recommendations without altering the composite workflow.

Dominant driver groups in the proposed framework are determined by the AHP weight structure rather than by a single indicator layer. The weighting assigns comparable overall influence to the topographic–geological and climatic–anthropogenic domains (0.40 each), with a smaller but meaningful contribution from the hydrological–ecological domain (0.20). At the indicator level, the model is most sensitive to slope- and accessibility-related pressures, including built-up and infrastructure proximity, as well as shoreline proximity. Lithology, SOC, and LST trend provide secondary modulation, whereas NDWI- and NDVI-related trends act as biophysical modifiers where persistent drying or vegetation decline is expressed. Fault proximity has the smallest global weight, reflecting its role as a contextual structural control that increases geological realism without dominating basin-wide patterns.

4.2. Process Interpretation of the Thematic Indices and Plausibility of Results

The topographic–geological component (TGRI) expresses terrain predisposition through slope steepness, lithological resistance, soil susceptibility (SOC), and structural setting. This configuration follows established process understanding for mountain environments, where steep gradients, weaker rock units, and structural discontinuities jointly condition slope instability and erosion-prone terrain. In the Charvak basin, elevated TGRI values along reservoir-facing escarpments and valley-side slopes therefore represent a plausible expression of background controls and are consistent with regional syntheses emphasizing lithological contrasts and tectonic structures (Khakimov *et al.*, 2024; Liu *et a*l., 2024; Caleca *et al.*, 2024; Fazilova *et al.*, 2025). Given its comparatively small global weight (Table 2), fault proximity is best interpreted as a local modulator (e.g., fracture-controlled weakening and slope segmentation) rather than a basin-wide driver.

The HERI captures reservoir influence and moisture-related change by combining shoreline proximity with NDWI trend risk. High HERI values in the nearshore belt are expected because shoreline distance proxies bank undercutting, saturation, and drawdown effects typical for regulated reservoirs. Away from the shoreline, NDWI trend risk refines the signal by highlighting areas where persistent moisture change contributes to ecological stress. To suppress shoreline-driven artifacts in the trend term, NDWI trend risk is excluded in the immediate nearshore band, whereas shoreline proximity governs the hydrological–ecological pressure in this zone (e.g., Wang *et al.*, 2024). This interpretation is consistent with reported effects of water level fluctuations on bank stability and riparian condition in mountain reservoirs (Juliev *et al.*, 2023; Fazilova *et al.*, 2026).

The CARI integrates vegetation-condition change (NDVI trend risk), built-up dynamics (NDBI trend risk), infrastructure proximity, and thermal stress (LST trend risk). Its corridor-focused pattern is plausible because accessibility concentrates development pressure, land cover modification, and associated heat and fragmentation effects, particularly around tourism and recreation zones. Colocation of higher CARI values with built-up growth hotspots and proximity to infrastructure aligns with evidence that land use intensification around reservoir margins and along major access routes can amplify ecological stress (Juliev *et al.*, 2019; Fazilova *et al.*, 2026). Including LST trend supports interpretation of CARI as a pressure index sensitive to warming-prone surfaces and land cover transitions.

Direct quantitative validation is constrained by limited inventories and field measurements; however, agreement between mapped thematic patterns and expected process behavior provides a first-order plausibility check. In addition, the relative influence implied by the AHP structure (Table 2) is consistent with the spatial signals: slope and built-up pressure have the largest global shares, with shoreline proximity and infrastructure proximity providing major additional contributions.

Recent ecological vulnerability studies provide the broader methodological context for such multifactor mapping, including AHP-based weighting frameworks (Hu *et a*l., 2021), remote-sensing driven vulnerability indices at regional scales (Wu *et al*., 2021), hybrid modeling strategies (Dossou *et a*l., 2021), and spatiotemporal evolution analyses across major plateaus and basins (Xia *et al*., 2021; Zhang *et al*., 2022; Zhang *et al*., 2025). Relative to these large-area applications—often dominated by broad climate–vegetation gradients and extensive land cover transitions—the Charvak basin exhibits a more localized signal shaped by reservoir shoreline processes and accessibility corridors. In this sense, the results remain consistent with corridor-related pressure patterns emphasized in vulnerability assessments that incorporate urbanization and infrastructure effects (Wu *et al*., 2021) while extending AHP-oriented mapping (Hu *et al*., 2021) through explicit reporting of domain subindices and a baseline-consistent near-term scenario stress test tailored to a reservoir-affected mountain basin.

4.3. Interpretation of the 2030 Scenario and Planning Implications

The 2030 maps represent a scenario-based stress test rather than a deterministic forecast. The near-term horizon (2030 relative to the 2023 baseline) is chosen to support actionable planning and to remain aligned with the 2018–2023 reference window. The scenario combines baseline-anchored extrapolation of land surface indicators with explicit stressors that emulate plausible intensification of shoreline influence and corridor-related pressure; accordingly, the outputs should be interpreted as spatial sensitivity to these assumptions, not as exact future states.

The scenario indicates that vulnerability increases most where multiple pressures co-occur on predisposed terrain. Shoreline-related stress expands the nearshore belt of elevated vulnerability, whereas accessible valleys respond primarily to infrastructure- and land use-related drivers. This supports a two-zone planning logic: (i) shoreline belts where reservoir-level dynamics may amplify bank processes and ecological stress, and (ii) access corridors where development pressure may intensify disturbance. The domain indices provide a driver-specific basis for interventions—shoreline monitoring and protection where HERI dominates, land use regulation where CARI dominates, and hazard-aware restrictions where high TGRI indicates strong predisposition—supporting ecosystem-oriented mitigation and spatial planning in the Charvak basin (Juliev *et al*., 2023; Fazilova *et al*., 2026).

From a water management perspective in Uzbekistan, the high-vulnerability shoreline belt is operationally relevant because seasonal drawdown and high-water phases can accelerate bank erosion and undercutting, affecting nearshore ecosystems and recreational assets; this motivates shoreline protection belts and targeted monitoring of erosion-prone segments. Hotspots along the main inflow valleys further indicate priority corridors where sediment delivery, slope processes, and infrastructure expansion may jointly increase management pressure, motivating coordinated monitoring and land use regulation (Juliev *et al*., 2023; Fazilova *et al*., 2026).

4.4. Limitations and Future Work

Several limitations should be noted. First, the magnitude and ranking of vulnerability depend on indicator selection, orientation-consistent normalization, and the AHP weighting scheme; reporting both the composite EVI and the domain subindices (TGRI, HERI, and CARI) partially mitigates this by improving transparency. Second, results are constrained by the spatial resolution and temporal availability of the input datasets, including mixed-resolution ancillary layers (e.g., SOC), and by limited independent inventories for quantitative validation of mapped hotspots. Coupled NDVI–LST drought metrics, such as the temperature–vegetation dryness index (TVDI) and the normalized temperature drought index (NTDI), were not computed; long-term NDVI and LST trends were used instead as separate, interpretable indicators. Additional soil predictors (e.g., soil moisture/texture/depth) were not included because of limited harmonized basin-scale layers; this is a key limitation for predictive interpretation. Third, the 2030 output denotes a scenario-based stress test rather than a deterministic forecast, as it depends on assumptions about short-term trend persistence and prescribed stress adjustments anchored to the baseline. Finally, some predictors act mainly as contextual controls (e.g., fault proximity); thus, local structural effects may be underrepresented where detailed geotechnical data are unavailable.

Future work should test multiple scenario settings for land use/tourism development and reservoir operation, and apply alternative time-series approaches (e.g., nonlinear trends and breakpoint detection) where linear extrapolation is not appropriate. Robustness can be strengthened through uncertainty and sensitivity analyses of key modeling choices (weights, normalization, and fixed class thresholds). Validation could be expanded using independent evidence such as documented shoreline-instability segments, land use change inventories, and targeted field observations in representative shoreline and corridor hotspots.

5. Conclusion

High–very high ecological vulnerability concentrates along the reservoir-facing escarpments of North Pskem and the southern Kenkol–Chatkal rim, whereas lower vulnerability prevails in the forested upper Pskem and parts of the South Ugam uplands. Hotspots occur where steep terrain and susceptible lithological settings coincide with shoreline influence and corridor-related anthropogenic pressure, particularly along the western waterfront and the main access valleys.

The weighting structure assigns equal overall influence to the topographic–geological and climatic–anthropogenic domains (0.40 each), whereas the hydrological–ecological domain contributes 0.20. At the indicator level, slope and built-up dynamics provide the strongest contributions, followed by shoreline proximity and proximity to infrastructure; lithology further modulates spatial patterns, whereas SOC and thermal-stress trends contribute as secondary susceptibility and pressure components.

Observed change between 2018 and 2023 is modest in terms of class transitions: the high–very high classes decrease slightly from 502.6 to 500.4 km^2 (−2.1 km^2; −0.2 percentage points). Under the 2030 combined-stress scenario (baseline 2023), the high–very high classes increase to 539.8 km^2 (+39.4 km^2; +3.2 percentage points), with expansion focused along shoreline-adjacent belts and major access corridors. Overall, the outputs support priority zoning, shoreline monitoring, and corridor-oriented land use management in reservoir-influenced mountain basins.

Acknowledgements

The authors would like to express their sincere gratitude to all parties who have contributed to the research and the completion of this manuscript. Special thanks are extended to mentors, funding institutions, and data providers for their invaluable support and assistance throughout the study.

Author Contributions

Conceptualization: Magdiev, K., Fazilova, D.; **methodology**: Fazilova, D.; **investigation**: Magdiev, K., Fazilova, D., Makhmudov, M.; **writing—original draft preparation**: Magdiev, K., Fazilova, D. Makhmudov, M.; **writing—review and editing**: Magdiev, K., Fazilova, D. Makhmudov, M.; **visualization**: Magdiev, K. All authors have read and agreed to the published version of the manuscript.

Conflict of interest

All authors declare that they have no conflicts of interest.

Data availability

Data are available upon re-quest.

Funding

This Research Was Funded by Agency of Innovative Development Under the Ministry of Higher Education, Science, And Innovation Of the Republic Of Uzbekistan, Grant Number Fl-8824063217.

References

Agli, S., Ahmed, A., Abdellah, A., Abdelouahed, F., Said, M., Abdelfattah, A., & Akram, E. G. (2024). Modelling of Soil Erosion Susceptibility Using the Multi-Influencing Factor Method in the Amizmiz Basin, Morocco. *Forum Geografi*, 38(3), 343–357. doi: 10.23917/forgeo.v38i3.6263

Aichi, A., et al. (2024). Integrated GIS and analytic hierarchy process for flood risk assessment in the Dades Wadi watershed (Central High Atlas, Morocco*). Results in Earth sciences*, 2, 100019. doi: 10.1016/j.rines.2024.100019

Alikhanov, B., Pulatov, B., & Samiev, L. (2024). The detection of past and future land use and land cover change in Ugam Chatkal National Park, Uzbekistan, using CA-Markov and Random Forest machine learning algorithms. *Forum Geografi,* 38(2), 121-137. doi: 10.23917/forgeo.v38i2.4221

Arif, N., & Toersilowati, L. (2024). Monitoring and predicting development of built-up area in sub-urban areas: A case study of Sleman, Yogyakarta, Indonesia. *Heliyon*. https://doi.org/10.1016/j.heliyon.2024.e34466

Caleca, F., Scaini, C., Frodella, W., & Tofani, V. (2024). Regional-scale landslide risk assessment in Central Asia. *Natural Hazards and Earth System Sciences*, 24, 13–27. https://doi.org/10.5194/nhess-24-13-2024

Chauhan, V., Gupta, L., Dixit, J. (2025). Landslide susceptibility assessment for Uttarakhand, a Himalayan state of India, using multi-criteria decision making, bivariate, and machine learning models. *Geoenvironmental Disasters*, 12(2). https://doi.org/10.1186/s40677-024-00307-3

Chen, J., Wang, Y., Wang, J., Zhang, Y., Xu, Y., Yang, O., Zhang, R., Wang, J., Wang, Z., Lu, F., & Hu, Z. (2024). The performance of Landsat-8 and Landsat-9 data for water body extraction based on various water indices: A comparative analysis. *Remote Sensing*, 16(11), 1984. doi: 10.3390/rs16111984

Chouari, W. (2024). Assessment of vegetation cover changes and the contributing factors in the Al-Ahsa Oasis using Normalized Difference Vegetation Index (NDVI). *Regional Sustainability*, 5(1), 100111. Doi: 10.1016/j.regsus.2024.03.005

Coelho, C. D., da Silva, D. D., Amorim, R. S. S., Vasconcelos, B. N. F., Possato, E. L., Filho, E. I. F., Brandão, P. C., Ferreira Neto, J. A., & Silva, L. V. (2024). Development and Application of an Environmental Vulnerability Index (EVI) for Identifying Priority Restoration Areas in the São Francisco River Basin, Brazil. *Land*, 13(9), 1475. doi: 10.3390/land13091475

Dainese, M., Crepaz, H., Bottarin, R., Fontana, V., Guariento, E., Hilpold, A., Obojes, N., Paniccia, C., Scotti, A., Seeber, J., Steinwandter, M., Tappeiner, U., Niedrist, G. (2024). Global change experiments in mountain ecosystems: A systematic review. *Ecological Monographs*, 94(4), e1632. doi: 10.1002/ecm.1632

Darabi, H., Haghighi, A. Klove, B., & Luoto, M. (2025). Remote sensing of vegetation trends: A review of methodological choices and sources of uncertainty. *Remote Sensing Applications: Society and Environment*, 37, 101500. doi: 10.1016/j.rsase.2025.101500

Ding, Y., Chen, G. (2025). Assessment of ecological environment quality and analysis of its driving forces in the Dabie Mountain Area of Anhui Province based on the improved Remote Sensing Ecological Index. *Sustainabilit*y, 17, 6198. doi: 10.3390/su17136198

Dossou, J. F., Li, X. X., Sadek, M., Sidi Almouctar, M. A., & Mostafa, E. (2021). Hybrid model for ecological vulnerability assessment in Benin. *Scientific Reports,* 11(1), 2449. doi: 10.1038/s41598-021-81742-2

Drummer, T.D. (1998). Generalized Geology of the Former Soviet Union (geo1ec). U.S. Geological Survey Data Release. doi: 10.5066/P9GUL0PQ

El Beyrouthy, N., Al Sayah, M., Der Sarkissian, R., & Nedjai, R. (2025). Enhancing Land Degradation Assessment Using Advanced Remote Sensing Techniques: A Case Study from the Loiret Region, France. *Land*, 14(12), 2439. doi: 10.3390/land14122439

Estacio, I., Lim, C., Onitsuka, K., Hoshino, S. (2024). Predicting the future through observations of the past: Concretizing the role of geosimulation for holistic geospatial knowledge. *Geomatica*, 76, 100012. doi: 10.1016/j.geomat.2024.100012

Estoque, R.C., Ishtiaque, A., Parajuli, J. (2023). Has the IPCC's revised vulnerability concept been well adopted? *Ambio* 52, 376–389. doi: 10.1007/s13280-022-01806-z

Fan, J., Meiliya, Y., & Wu, S. (2025). Landslide Risk Assessment in the Xiluodu Reservoir Area Using an Integrated Certainty Factor–Logistic Regression Model. *Geomatics*, 5(4), 59. doi: 10.3390/geomatics5040059

Fazilova, D., Magdiev, Kh., Makhmudov, M., Kabilov, Kh. (2026). Lineament analysis and water level variations in the geodynamic assessment of the Charvak Reservoir Area, Uzbekistan (2022–2024). *International Journal of Engineering and Geosciences*, 11(1), 89–105. doi: 10.26833/ijeg.1652490

Fazilova, D., Magdiev, K., Rakhimberdieva, M. (2025). GIS and lineament analysis for monitoring geodynamic activity in the Charvak Reservoir Region. *International Journal of Geoinformatics*, 21(7), 47–57. doi: 10.52939/ijg.v21i7.4317

Fazilova, D., Magdiev, K., & Sichugova, L. V. (2021). Vertical accuracy assessment of open access digital elevation models using GPS. *International Journal of Geoinformatics*, 17(1), 19–26. doi: 10.52939/ijg.v17i1.1701

Fornasaro, S., Ghezzi, L., Arrighi, S., Shukurov, N., Petrov, M., Tomei, A., & Petrini, R. (2025). Geochemistry and risk assessment of potentially toxic elements in surface river sediments (Chirchik-Akhangaran basin, Uzbekistan). *Environ Geochem Health*, 47, 127. doi: 10.1007/s10653-025-02441-9

Fornasaro, S., Ghezzi, L., Shukurov, N. (2024) Water quality and dissolved load in the Chirchik and Akhangaran river basins (Uzbekistan, Central Asia). *Environ Monit Assess*, 196, 854. doi: 10.1007/s10661-024-13014-1

Guo, B., Xu, M., Zhang, R. (2024). A new monitoring index for ecological vulnerability and its application in the Yellow River Basin, China from 2000 to 2022. *J. Arid Land* 16, 1163–1182. doi: 10.1007/s40333-024-0106-z

Hasan, I., Goni, O., Katha, Z.T. et al. (2025). Prediction modeling of land surface temperature in relation to land cover dynamics and health risk perception analysis in barishal city of Bangladesh. *Sci Rep* 15, 30730. doi: 10.1038/s41598-025-14868-2

Hengl, T., & Wheeler, I. (2018*). Soil organic carbon content in × 5 g/kg at 6 standard depths (0, 10, 30, 60, 100 and 200 cm) at 250 m resolution (*Version v02) [Data set]. Zenodo. doi: 10.5281/zenodo.1475457

Hu, X., Ma, C., Huang, P., & Guo, X. (2021). Ecological vulnerability assessment based on AHP-PSR method and analysis of its single parameter sensitivity and spatial autocorrelation for ecological protection–A case of Weifang City, China. *Ecological Indicators*, 125, 107464. doi: 10.1016/j.ecolind.2021.107464

Hyman, A.A., Crone, E.R., Benson, A., Dunham, J., Lynch, A.J., Thompson, L., Mims, M.C. (2025). Exposure, sensitivity, or adaptive capacity? Reviewing assessments that use only two of three elements of climate change vulnerability. *Conservation Science and Practice*, 7(1), e13293. doi: 10.1111/csp2.13293

Jia, Y., Li, Z., Gao, H., Wang, S., Sun, M., & Wang, P. (2024). Hydrological response to climate change in a glacierized catchment in eastern Tien Shan, Central Asia. Journal of Hydrology: *Regional Studies*, 51, 101669. doi: 10.1016/j.ejrh.2024.101669

Juliev, M., Ng, W., Mondal, I., Begimkulov, D., Gafurova, L., Hakimova, M., Ergasheva, O., Saidova, M. (2023). Surface displacement detection using object-based image analysis, Tashkent region, Uzbekistan. *E3S Web of Conferences,* 386, 04010. doi: 10.1051/e3sconf/202338604010

Juliev, M., Pulatov, A., Fuchs, S., Hübl, J. (2019). Analysis of land use land cover change detection of Bostanlik District, Uzbekistan. *Polish Journal of Environmental Studies*, 28(5), 3235–3242. doi: 10.15244/pjoes/94216

Kamran, M., Yamamoto, K. (2023). Evolution and use of remote sensing in ecological vulnerability assessment: A review. *Ecological Indicators*, 148, 110099. doi: 10.1016/j.ecolind.2023.110099

Kassahun, M. T., & Workineh, N. A. (2025). Land Surface Temperature Retrieval from Landsat 9 Satellite Data in the Case of Injibara Town and the Surrounding Banja District, Awi Nationality Administrative Zone, Amhara, Ethiopia. *Forum Geografi*, 39(2), 125–135. doi: 10.23917/forgeo.v39i2.6363

Khakimov, K.A., Janizakova, G.M., Sharipov, S.M., Safarov, E., Boymurodov, D.O. (2024). Exploring the classification, dynamics, and control measures of landslide processes in the Charvak Free Tourist Zone. In: *Proceedings of the 2nd Pamir Transboundary Conference for Sustainable Societies (PAMIR-2 2023)*, 1033–1036. SCITEPRESS – Science and Technology Publications.

Khuc, T., Truong, X., Tran, V., Bui, D., Bui, D., Ha, H., Tran, T., Pham, T., Yordanov, V. (2023). Comparison of multi-criteria decision making, statistics, and machine learning models for landslide susceptibility mapping in Van Yen District, Vietnam. *International Journal of Geoinformatics*, 19(7), 33–45. doi: 10.52939/ijg.v19i7.2743

Kurnianto, F. A., Nurdin, E. A., Pangastuti, E. I., & Bella, S. (2024). Monitoring Mining Impact for Geosites Using Time Series NDVI and Runoff in the Eastern Part of Southern Java Mountains, Indonesia. *Forum Geografi*, 38(2), 291-301. doi: 10.23917/forgeo.v38i2.2996

Li, J., Chen, Y., Gu, Y., Wang, M., & Zhao, Y. (2024). Remote Sensing Mapping and Analysis of Spatiotemporal Patterns of Land Use and Cover Change in the Helong Region of the Loess Plateau Region (1986–2020). *Remote Sensing*, 16(19), 3738. doi: 10.3390/rs16193738

Liao, Z., et al. (2022). Identifying the essential conditioning factors of landslide susceptibility models: A case study in Wanzhou, Three Gorges Reservoir, China. *Catena,* 217, 106428. doi: 10.1016/j.catena.2022.106428

Liu, X., Shao, S. & Shao, S. (2024). Landslide susceptibility zonation using the analytical hierarchy process (AHP) in the Great Xi'an Region, China. *Scientific Reports*, 14, 294. doi: 10.1038/s41598-024-53630-y

Luo, Q., Bao, Y., Wang, Z., Chen, X., Wei, W., Fang, Z. (2023). Vulnerability assessment of urban remnant mountain ecosystems based on ecological sensitivity and ecosystem services. *Ecological Indicators*, 151, 110314. doi: 10.1016/j.ecolind.2023.110314

Mandal, P., Mukhopadhyay, A., Mukherjee, S. (2023) Assessing the suitability of a reservoir site in a water-stressed area in Purulia, India, using AHP-TOPSIS. *Sustain. Water Resour. Manag*. 9, 74. doi: 10.1007/s40899-023-00852-z

Miura, Y., Shamsudduha, M., Suppasri, A. (2025). A Global Multi-Sensor Dataset of Surface Water Indices from Landsat-8 and Sentinel-2 Satellite Measurements. *Sci Data,* 12, 1253. doi: 10.1038/s41597-025-05562-z

Muro, J., Strauch, A., Heinemann, S., Steinbach, S., Thonfeld, F., Waske, B., & Diekkrüger, B. (2018). Land surface temperature trends as indicator of land use changes in wetlands. *International Journal of Applied Earth Observation and Geoinformation, 70*, 62–71. doi: 10.1016/j.jag.2018.02.002

NASA Shuttle Radar Topography Mission (SRTM). (2013). *Shuttle Radar Topography Mission (SRTM) Global.* Distributed by OpenTopography. [Accessed 2025-09-26].

Niyogakiza, A., & Liu, Q. (2025). GIS-Driven Multi-Criteria Assessment of Rural Settlement Patterns and Attributes in Rwanda's Western Highlands (Central Africa). *Sustainability*, 17(14), 6406. doi: 10.3390/su17146406

Pachore, A., Agrawal, N., Omonov, N., Rakhmonov, K., Umirzakov, G., Mujumdar, S., Remesan, R. (2024). Evaluation of the impact of anthropogenic storage on the hydrological drought propagation in two contrasting semi-arid river basins. *Journal of Water and Climate Change*, 15(7), 3276–3292. doi: 10.2166/wcc.2024.105

Rehman, A., Sajjad, M., Song, J., Riaz, M.T., Mehmood, M.S., Ahamad, M.I. (2024). Integrated frequency ratio–analytical hierarchy and geospatial techniques-based earthquake risk assessment in mountainous cities: A case from the Northwestern Himalayas. *Georisk*, 19(2), 389–409. doi: 10.1080/17499518.2024.2378285

Rosi, A., Frodella, W., Nocentini, N., Caleca, F., Havenith, H. B., Strom, A., Saidov, M., Bimurzaev, G. A., & Tofani, V. (2023). Comprehensive landslide susceptibility map of Central Asia. *Natural Hazards and Earth System Sciences*, 23, 2229–2250. doi: 10.5194/nhess-23-2229-2023

Saaty, T. L. (2008). Decision making with the analytic hierarchy process. *International Journal of Services Sciences*, 1(1), 83–98. doi: 10.1504/IJSSCI.2008.017590

Saha, S., Das, S., Maiti, R. (2022). Multi-model comparison of soil erosion risk mapping using RUSLE, AHP, and machine learning in eastern India. Regional Sustainability, 3(2), 135–147. doi: 10.1016/j.regsus.2022.06.003

Salgado, L., González, L. M., Gallego, J. L. R., López-Sánchez, C. A., Colina, A., & Forján, R. (2025). Mapping Soil Organic Carbon in Degraded Ecosystems Through Upscaled Multispectral Unmanned Aerial Vehicle–Satellite Imagery. *Land*, 14(2), 377. doi: 10.3390/land14020377

Salokhiddinov, A., Juliev, M., Mirzaqobulov, J., Khakimova, P., Khomidov, A., & Abdikairov, B. (2025). Bibliometric mapping of research on water availability in Central Asia. *Forum Geografi*, 39(2), 262–273. doi: 10.23917/forgeo.v39i2.8991

Samsuddin, N., Salleh, S. A., Khalid, N., Saraf, N. M., Yaman, R., Pintor, L., Rueda, G., & Samsuddin, N. (2025). Assessing the Heat Vulnerability Index (HVI) in Klang Valley Using Principal Component Analysis (PCA) and an Equal-Weighted Approach. *Forum Geografi*, 39(2), 188–208. doi: 10.23917/forgeo.v39i2.8633

Tacconi Stefanelli, C., Frodella, W., Caleca, F., Raimbekova, Z., Umaraliev, R., & Tofani, V. (2024). Assessing landslide damming susceptibility in Central Asia. *Natural Hazards and Earth System Sciences*, 24, 1697–1720. doi: 10.5194/nhess-24-1697-2024

Taoukidou, N., Karpouzos, D., & Georgiou, P. (2025). Flood Hazard Assessment Through AHP, Fuzzy AHP, and Frequency Ratio Methods: A Comparative Analysis. *Water*, 17(14), 2155. https://doi.org/10.3390/w17142155

Tesfaye, M., et al. (2024). Performance of water indices for large-scale water resources assessment in Ethiopia. *Environmental Monitoring and Assessment,* 196, 467. doi: 10.1007/s10661-024-12630-1

Terán-Gómez, V. F., Buitrago-Ramírez, A. M., Echeverri-Sánchez, A. F., Figueroa-Casas, A., & Benavides-Bolaños, J. A. (2025). Integrating AHP and GIS for Sustainable Surface Water Planning: Identifying Vulnerability to Agricultural Diffuse Pollution in the Guachal River Watershed. *Sustainability*, 17(9), 4130. doi:10.3390/su17094130

Tsay, O. (2019). Electronic map of faults of the Middle, Southern Tien Shan and adjacent territories. In: Proceedings of the LI Tectonic Meeting “Fundamental Problems of Tectonics and Geodynamics”, 2, 382–386.

Ullah, N., Tariq, A., Qasim, S., Panezai, S., Uddin, M. G., Abdullah-Al-Wadud, M., & Ullah, S. (2024). Geospatial analysis and AHP for flood risk mapping in Quetta, Pakistan: A tool for disaster management and mitigation. *Applied Water Science*, 14, Article 236. doi: 10.1007/s13201-024-02293-1

U.S. Geological Survey. (2024). *Landsat Collection 2 Surface Reflectance*. Retrieved From https://www.usgs.gov/landsat-missions/landsat-collection-2-surface-reflectance

Wang, X., Ma, X., Guo, D., Yuan, G., & Huang, Z. (2024). Construction and optimization of landslide susceptibility assessment model based on machine learning. *Applied Sciences*, 14(14), 6040. doi: 10.3390/app14146040

Wei, H., Zhang, Q., Liu, Y. (2023). Mountain ecosystem service assessment and vulnerability zoning with AHP-GIS: roles of slope, NDVI, rainfall, and evapotranspiration. *Regional Sustainability*, 4(1), 45–57. doi: 10.1016/j.regsus.2023.02.004

Wu, H., Guo, B., Fan, J., Yang, F., Han, B., Wei, C., Lu, Y., Zang, W., Zhen, X., & Meng, C. (2021). A novel remote sensing ecological vulnerability index on large scale: A case study of the China-Pakistan Economic Corridor region. *Ecological Indicators,* 129, 107955. doi: 10.1016/j.ecolind.2021.107955

Wu, S., Zhang, Y., & Yan, J. (2022). Comprehensive Assessment of Geopolitical Risk in the Himalayan Region Based on the Grid Scale. *Sustainability*, 14(15), 9743. doi: 10.3390/su14159743

Xia, M., Jia, K., Zhao, W., Liu, S., Wei, X., & Wang, B. (2021). Spatio-temporal changes of ecological vulnerability across the Qinghai-Tibetan Plateau. *Ecological Indicators*, 123, 107274. doi: 10.1016/j.ecolind.2020.107274

Xu, E., Zhang, G., Wang, H., Yang, M., Tian, H., Zhao, M., Dong, N., Li, C., Hu, Y., Tian, G. (2025). Monitoring and Assessing Ecological Environmental Quality in Qianping Reservoir, Central China: A Remote Sensing Ecological Index (RSEI) *Approach. Forests*, 16(5):831. doi: 10.3390/f16050831

Xu, H., Ren, M., & Lin, M. (2024). Cross-comparison of Landsat-8 and Landsat-9 data: A three-level approach based on underfly images. *GIScience & Remote Sensing*, 61(1), 2318071. https://doi.org/10.1080/15481603.2024.2318071

Ye, Y., Wang, Y., Liao, J., Chen, J., Zou, Y., Liu, Y., Feng, C. (2022). Spatiotemporal Pattern Analysis of Land Use Functions in Contiguous Coastal Cities Based on Long-Term Time Series Remote Sensing Data: A Case Study of Bohai Sea Region, China. *Remote Sensing*, 14(15):3518. doi: 10.3390/rs14153518

Yu, F., Li, C., Yuan, Z., Luo, Y., Yin, Q., Wang, Q., Hao, Z. (2023). How do mountain ecosystem services respond to changes in vegetation and climate? Evidence from the Qinling Mountains, China. *Ecological Indicators*, 154, 110922. doi: 10.1016/j.ecolind.2023.110922

Yun, X., Wang, J., & Bao, H. (2025). Assessing climate change impacts on extreme hydrological characteristics of reservoir inflow in Tianshan Mountain Range, China. *Scientific Reports*, 15, 14925. doi: 10.1038/s41598-025-98651-3

Zhang, X., Liu, K., Wang, S., Wu, T., Li, X., Wang, J., Wang, D., Zhu, H., Tan, C., & Ji, Y. (2022). Spatiotemporal evolution of ecological vulnerability in the Yellow River Basin under ecological restoration initiatives. *Ecological Indicators*, 135, 108586. doi: 10.1016/j.ecolind.2022.108586

Zhang, X., Zheng, Y., Yang, Y., Ren, H., & Liu, J. (2025). Spatiotemporal evolution of ecological vulnerability on the Loess Plateau. *Ecological Indicators,* 170, 113060. doi: 10.1016/j.ecolind.2024.113060

Zhou, Y., Dong, J., Xiao, X., Xiao, T., Yang, Z., Zhao, G., Zou, Z., & Qin, Y. (2017). Open surface water mapping algorithms: A comparison of water-related spectral indices and sensors. *Water,* 9(4), 256. doi: 10.3390/w9040256

Zhu, Y., Sang, F., Wang, B., Lutz, A., Hu, S., Chen, D., & Singh, V. P. (2023). Heterogeneity in Spatiotemporal Variability of High Mountain Asia's Runoff and Its Underlying Mechanisms. *Water Resources Research*, 59(7), e2022WR032721. doi: 10.1029/2022WR032721